FULL RESEARCH ARTICLE

Mechanical properties of lightweight 3D-printed structures made with carbon-filled nylon

Roberto Spina[1,2,3] ⬤ · Luigi Morfini[1,2] · Luigi M. Galantucci[1]

Abstract

Material extrusion additive manufacturing is a widely used 3D-printing process involving depositing molten thermoplastic materials layer by layer to create a 3D object. Combining material extrusion with composites creates strong, lightweight, and functional parts with unique properties. This study uses chopped carbon fiber reinforcement to investigate polyamide's thermal, rheological, and mechanical properties. The study includes an analysis of the material's thermal properties via differential scanning calorimetry and its flow behavior via rotational rheometry. This study provides a comprehensive understanding of carbon-filled nylon PA material's economic and mechanical properties, which will help optimize its performance for various applications. Tensile and flexural tests were used to appraise the material's strength and stiffness under different loading conditions. A cost analysis was performed to compute the specimen cost as a function of orientation and infill density. The aim was to understand how the type and strategy of infill design impact the material's mechanical properties, helping optimize the performance of components and evaluating its cost.

1 Introduction

Composite materials with a high percentage of fillers have recently become of great interest in material extrusion (MEX) additive manufacturing (AM) due to nozzle-based technologies, such as fused filament fabrication (FFF) [1], continuous filament fabrication (CFF) and continuous fiber reinforcement (CFR) [2], automated fiber placement (AFP) and automated tape laying (ATL) [3]. AFP/ATL can be classified as a material extrusion process using fiber-polymer tape as feedstock with the same layer-by-layer manufacturing methodology based on the deposition in a layer-wise manner [4]. These technologies take their design cues from MEX in that there is a head that deposits material. Still, at the same time, they differ, because they allow the fabrication of components made of composite material. Specifically, printers with CFR technology possess two nozzles assigned to printing: one dedicated to manufacturing the polymeric matrix and the other to depositing the continuous fiber reinforcement [5]. These materials find use in various industries such as automotive, mechanical engineering, biomedical, and aviation.

Carbon fiber-reinforced polymers (CFRP) are of most significant interest for metal replacement applications [6–8]. Adding carbon fiber gives the material superior mechanical performance to its polymer counterparts. Many researchers have tested CFRP structures with continuous carbon fiber as reinforcement and achieved good results regarding tensile properties. The use of continuous fiber reinforcement further elevates the mechanical properties by having a material consisting of a composite matrix and a continuous fiber reinforcement [6, 9, 10]. Several reinforcement techniques have been developed, such as optimizing the printing parameters, adding fibrous and powdered material into the printed polymer, and applying post-processing treatments [11].

The ability to manufacture lightweight composite components is highly desirable as it offers numerous advantages to exploit. Lubombo [12] studied lightened

✉ Roberto Spina
   roberto.spina@poliba.it

1   Dipartimento di Meccanica, Matematica e Management, Politecnico di Bari, Bari, Italy

2   Istituto Nazionale di Fisica Nucleare (INFN)-Sezione di Bari, Bari, Italy

3   Consiglio Nazionale delle Ricerche-Istituto di Fotonica e Nanotecnologie (CNR-IFN), Bari, Italy

structures, analyzing the tensile and flexural properties of 3D-printed parts with five infill patterns. The square infill structure had the best tensile and strength, while the hexagonal infill exhibited the best flexural modulus and strength. Using numerical and experimental approaches, Dorčiak et al. [13] examined how the size and shape of inner structures affect the mechanical properties of 3D-printed constructions. The results proved that increasing the volume structure improved the mechanical properties, and a square shape infill type was the most effective. Bárnik et al. [14] analyzed hexagonal, triangular, and rectangular structures using tensile tests, identifying that the rectangular infill increased ultimate load force per unit volume compared to the other infill types. Moreover, specimens with higher infill densities yielded higher ultimate tensile loads. Ahmadifar et al. [15] conducted experiments on tensiles with different printing conditions. The study evaluated the effect of infill patterns (triangular, rectangular, hexagonal, and solid) on tensile strength, demonstrating that the solid infill pattern had the highest tensile strength. In contrast, the triangular infill pattern had the lowest. Changing the infill pattern to rectangular or hexagonal slightly improved the tensile strength. The hexagonal infill was also a topic of interest in AM due to its unique properties and potential applications [16, 17]. Researchers conducted numerous studies to investigate the effects of varying the dimensions and parameters of hexagonal cells on the mechanical and thermal properties of 3D-printed objects. Pipalla et al. [18] observed that the number of hexagon cells decreased with the increase in the thickness and length of the cell. The study found that the void space and weight significantly impact mechanical properties. Wang et al. [19] investigated the effects of infill pattern, infill density, and strain rate on the mechanical properties of 3D-printed composite structures. The results showed that the infill pattern significantly affected deformation and failure modes, and composites with hexagonal units had higher tensile modulus and strength. Increasing infill density improved strength. Strain rate affected stiffness, but imperfections dominated deformation and failure modes. The build orientation of a 3D-printed component also impacted mechanical properties, because the direction of depositing layers affected the anisotropy of the material, resulting in different levels of strength and stiffness. According to Ali et al. [20], the on-edge build direction showed higher tensile strength and Young's modulus but lower toughness than flat build direction composites. Secondary operations were also essential to improve the quality of manufactured parts and surface structuring to improve tribological properties, with reduced or no supplementary investments in machinery or production steps [21].

This work analyzes the material's thermal, rheological, and mechanical properties of the Nylon PA6 matrix and chopped carbon fiber reinforcement. The material was initially characterized with differential scanning calorimetry (DSC) to measure its thermal properties, such as glass transition and melting temperatures. Rheometer tests then allowed the evaluation of the material's flow behavior and viscosity under different conditions. Furthermore, the study investigated the changes in mechanical properties with various infill patterns (hexagonal, triangular, gyroids, rectangular) and building directions (*XY*/flat, *XZ*/on-edge) at a constant infill density. Tensile and flexural tests were used to appraise the material's strength and stiffness under different loading conditions. A cost analysis was performed to compute the specimen cost as a function of orientation and infill density. The aim was to understand how the type and strategy of infill design impact the material's mechanical properties, helping optimize the performance of components and evaluating its cost. The remainder of the manuscript is organized as follows. Section 2 describes the material and methods used to characterize it. In particular, the material characterization is functional to the following experimental study of material deposition. The deposition pattern is also investigated, evaluating the dimensional quality and the accuracy of the produced samples. The result section initially discusses the accuracy of the developed model. Section 3 reports the results of the mechanical tests and their statistical analysis. Finally, the outcomes of the statistical analysis are compared.

2 Materials and methods

The carbon-filled polyamide (PA) used in the investigation was the Onyx (Markforged Inc., USA), a proprietary material with a 1.75 mm filament diameter. The main properties were a nominal density of 1.2 g/cm^3, filled with 10.5% volume of chopped carbon microfiber [22]. The chopped fiber has a high variation in length (168 ± 37 μm) within the micrometer, as measured with laboratory facilities. It offered good mechanical properties, wear, and chemical resistance for parts with a high-quality surface finish and high heat tolerance [23]. The supplier declared an ultimate tensile strength (UTS) of 70 MPa and a tensile strain at break of 25% when printed with 100% filler [22].

The material's thermal properties were analyzed via DSC, and its viscosity at the printing temperature was analyzed via a rotational rheometer. A DSC 403 F1 Pegasus (Netzsch-Gerätebau GmbH, Selb, Germany), equipped with a silver furnace, was used for the thermal analysis of filaments in the supplied state and extruded from the nozzle. The samples of a few micrograms were placed in pure aluminum pans under a nitrogen atmosphere from ambient temperature to the maximum temperature of 300 °C with heating and cooling rates equal to 10 °C/min.

Rheological analyses were conducted using a HAAKE Mars III rheometer (Thermo Fisher Scientific Inc., MA, USA) with parallel-plate geometry with a plate diameter of 20 mm. Frequency sweep tests were performed with a strain amplitude of 1.0% to ensure a rheological behavior in the linear viscoelastic region, varying frequencies from 0.1 to 100 s^{-1}. The plate gap was kept constant at 0.5 mm during the test. The rheological properties of the Onyx were determined at different temperatures, from 230 to 270 °C, using a new sample for each test to ensure no thermal degradation occurred and starting at 120 s after inserting it between the plates. All the measurements were repeated in the air five times, with each test lasting 3 min to check reproducibility. Under these experimental conditions, the morphology of Onyx was stable, as verified before and after measurements. The time–temperature superposition (TTS) principle shifted frequency data into a single master curve at the investigated temperature of 275 °C.

Mark Two (Markforged Inc., USA) produced the samples. The spool was stored in a dry box to avoid moisture absorption, because it was a highly hygroscopic material. Based on FFF and CFR technology, the main features of this desktop series printer were a fully enclosed build volume of $320 \times 132 \times 154$ mm^3 and two independent nozzles, one designed for FFF printing and one for CFR printing. On the other hand, some significant limitations arose with this printer, such as the printing speed and nozzle temperature being predetermined and being unable to be changed. The build platform could not be heated. The printer also used the proprietary slicer Eiger™, optimized to be user-friendly. The slicer software selected the printing temperature of 275 °C and a specific printer speed unknown to the operator. Additional main parameters fixed for this study were:

The diameter of the FFF nozzle was 0.4 mm.
The layer height was 0.125 mm.
The number of wall layers was equal to 2.
The number of top/bottom layers was equal to 2.
The infill percentage was greater than 60%.

The choice to set the infill percentage was made considering that the infill density commonly affected the part strength. Standard 3D components subjected to light usage and limited strength to the maximum were realized with an infill percentage between 15% and 50%. This range of infill density provided a limited degree of strength by reinforcing the part structure without adding significant weight or print time. Functional parts withstanding higher forces and loads required a higher infill density, typically higher than 50%, to avoid ruptures under pressure. The choice of 100% infill density gave the best performance, but the part fabrication was long, and much material was used. The lower the infill percentage, the less material was used, and thus, the cheaper the part cost was.

Tensile tests were carried out on type 1B specimen, according to ISO 527:2019—plastics—determination of tensile properties, which dimensions are reported in Fig. 1. Prismatic samples of dimensions $80 \times 10 \times 4$ mm^3 were used for flexural tests following the ISO 178:2019—Plastics— Determination of flexural properties. Before mechanical testing, all specimens were inspected using optical and contact techniques to appraise their dimensional quality. A digital microscope, RH-2000 (Hirox Europe, Limonest, France), with a 1920×1200 pixels CMOS camera, captured images at 50 fps to measure the deposited line and evaluate the quality of the inner structure of the samples. A coordinate measurement machine (CMM) DeMeet 400 (Schut Geometrische Meettechniek bv, The Netherlands), with a standard Renishaw TP20 system with a 2 mm diameter stylus, was also used to measure the macro geometry. All measurements were conducted in a temperature-controlled environment, with a maximum variation of ± 0.5 °C from the ambient temperature. Mechanical tests were conducted on an eSun 10 universal testing machine (Galdabini, Italy) with a 100 kN load cell.

A mixed design of experiment (DoE) allowed the study of the effect of some specific parameters on mechanical behavior. Investigated factors were the printing orientation (the specimen position on the build platform) and the infill pattern. The printing orientation had two levels: *XY* (flat) and *XZ* (on-edge). On the other hand, the infill pattern had four levels: gyroid, hexagonal, rectangular, and triangular. Three replications were made for each combination of factors, and 24 specimens were obtained for tensile tests and 24 for flexural tests. The specimens were weighed, and their dimensional accuracy was initially evaluated with a
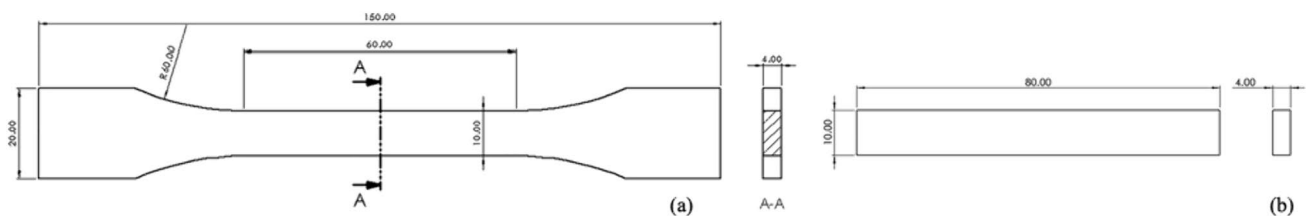

Fig. 1 Tensile specimen (**a**) and flexural specimen (**b**) (all dimensions in mm)

caliper and then with the CMM. The infill density of the tensile (Table 1) and flexural samples (Table 2) was calculated through the actual weight and plastic volume, a quantity computed by the Eiger slicer, representing the volume of material the specimen was made of. From Tables 1 and 2, the weight of the samples was different, as well as the amount of plastic used, due to the diversity of the filling cells selected for testing (Fig. 2), but the infill density was almost the same. At the same infill density, different filling cells required more material. This behavior was then reflected in the mechanical tests, where some fillings were better optimized despite lower material consumption,

resulting in superior mechanical characteristics. The difference in weight due to the orientation was associated with the different extensions of the top/bottom layers. This condition was particularly evident when analyzing the fully dense flexural samples, in which the difference in weight was 0.44 g.

Table 1 Tensile specimens

Specimen ID	Build orientation	Plastic volume (cm^3)	Weight (g)	Infill density (%)
Full *XY*	Flat	8.27	9.92	100.00
Full *XZ*	On-edge	8.81	10.57	100.00
Gyroid *XY*	Flat	5.37	6.44	64.93
Gyroid *XZ*	On-edge	5.68	6.82	64.47
Hexagonal *XY*	Flat	5.43	6.52	65.56
Hexagonal *XZ*	On-edge	5.56	6.67	63.11
Rectangular *XY*	Flat	5.38	6.46	65.06
Rectangular *XZ*	On-edge	5.52	6.62	62.66
Triangular *XY*	Flat	5.32	6.38	64.33
Triangular *XZ*	On-edge	5.54	6.65	62.88

Table 2 Flexural specimens

Specimen ID	Build orientation	Plastic volume (cm^3)	Weight (g)	Infill density (%)
Full *XY*	Flat	3.22	3.86	100.00
Full *XZ*	On-edge	4.10	3.42	100.00
Gyroid *XY*	Flat	2.07	2.48	64.29
Gyroid *XZ*	On-edge	2.19	2.58	62.87
Hexagonal *XY*	Flat	2.03	2.44	63.04
Hexagonal *XZ*	On-edge	2.19	2.63	64.04
Rectangular *XY*	Flat	2.09	2.51	64.91
Rectangular *XZ*	On-edge	2.17	2.60	63.45
Triangular *XY*	Flat	2.09	2.51	64.91
Triangular *XZ*	On-edge	2.09	2.51	61.11
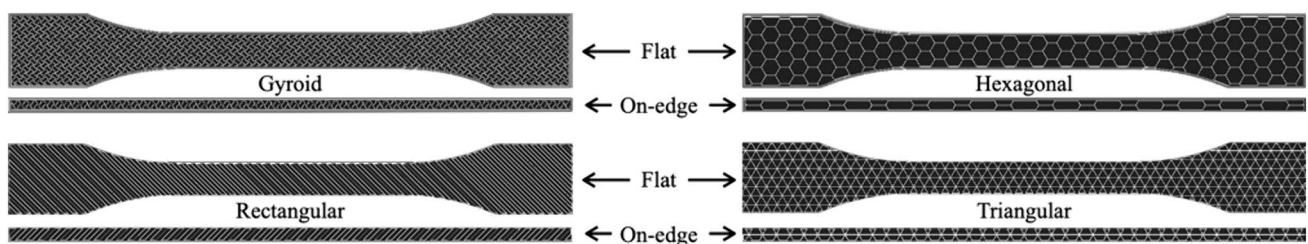
Fig. 2 Detail of printing orientation and infill strategies

3 Results and discussion

3.1 DSC and rheological analysis

The properties of carbon-filled PA were highly dependent on processing conditions, such as humidity, temperature, shear rates, and processing time [24]. The DSC analysis and rheometry were employed to assess the thermal and flow properties of the Onyx material in the MEX process. This analysis was crucial to measuring effective thermal properties, considering that additives could influence them [25].

The maximum temperature of the DSC analysis was set to 320 °C to repeat the cycle two times, avoiding the material decomposition occurring at higher temperatures. The degree of crystallinity X_c was calculated as

$$X_c = \frac{\Delta H_m - \Delta H_{cc}}{\Delta H_{m0}}, \tag{1}$$

where ΔH_m is the melting enthalpy at the melting temperature T_m, ΔH_{cc} is the cold crystallization enthalpy, and $\Delta H_{m,0}$ is the melting enthalpy for a complete crystalline material at the reference temperature T_{m0}. This last value of enthalpy was equal to 196 J×g^{-1} [26]. Figure 3 reports the DSC thermograms of the filament. The glass transition temperature T_g and melting temperature T_m were 100.2 °C and 201.5 °C, respectively. The melting enthalpy was 38.57 J×g^{-1}, with a crystallinity of 48%. No cold crystallization was detected. The crystallization temperature T_c was 160.3 °C. Based on the result of the DSC test, in the context of the dynamic scenario of MEX, the thermal behavior of Onyx affected the deposition and, hence, the performance of the final component. The material was considered fully melted at the extrusion temperature of 275 °C, maintaining its thermal stability for the two consecutive runs. No appreciable variations were detected in the main thermal properties.

The rheological characterization was performed to achieve relevant information for evaluating the MEX process. The viscoelastic behavior of the polymer influenced the melt extrusion through the nozzle and following welding of deposited layers. Viscoelastic functions such as storage modulus G', loss modulus G'', and complex viscosity η^* were measured from 230 to 290 °C (Fig. 4). The material seemed to obey the linear viscoelasticity models, with G' and G'' proportional to ω^2 and ω at low ω, respectively. The material showed almost a linear Newtonian melt behavior over the experimental frequency and temperature ranges, typical of a PA6. The temperature had an important effect on the rheological properties, especially at high shear rates. The apparent viscosity η^* significantly but steadily decreased over the investigated frequency range. The rigid carbon fibers in the nylon matrix probably contributed to orientation under shear force, disturbing the arrangement of the polymer chain entanglements and causing the strong shear thinning behavior (Fig. 5). These curves were then fitted, and the master curve was computed at the reference temperature of 275 °C. The intersection between G' and G'' was identified for an angular frequency of 628 rad/s.
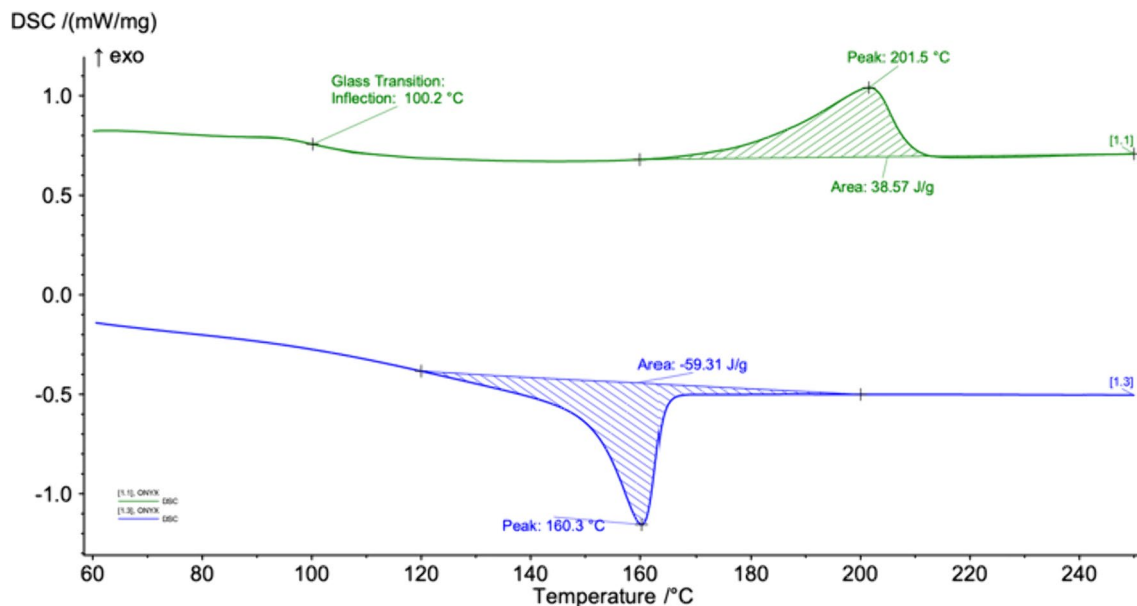

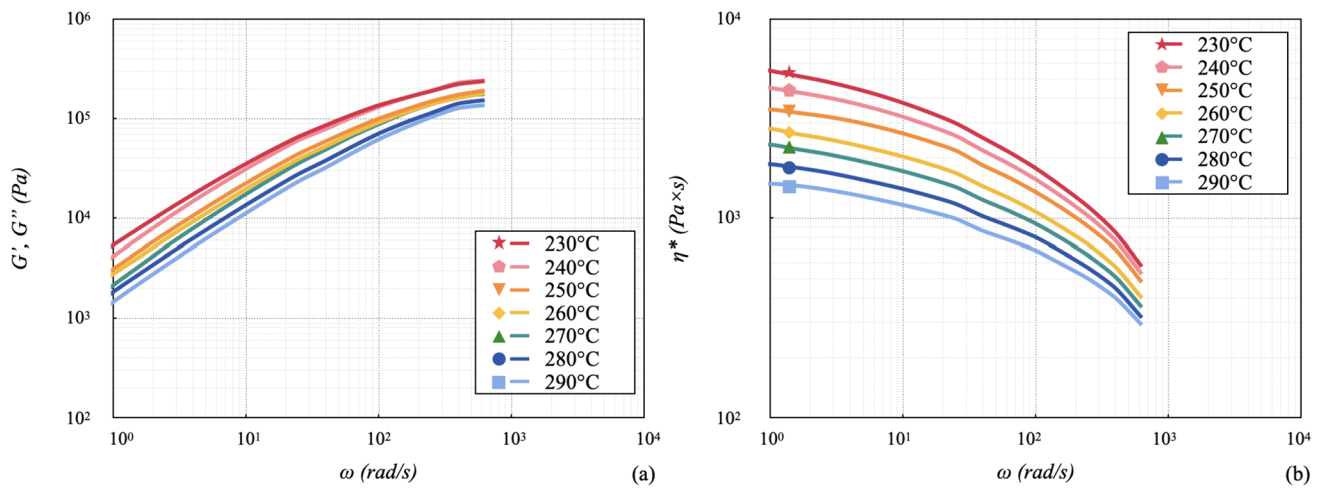
Fig. 3 DSC thermograms (heat flux vs. temperature)

Fig. 4 Storage G', loss G'' moduli (**a**), and apparent viscosity η^* (**b**)
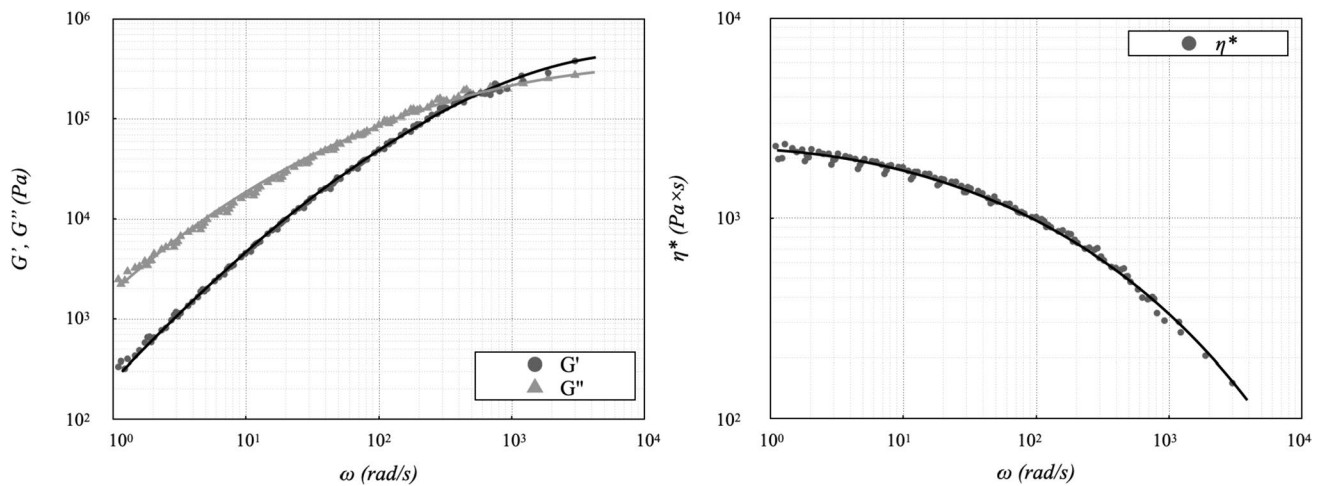

Fig. 5 Master curves at 275 °C computed with TTS

The other individual frequency data sets at different temperatures were shifted horizontally and vertically towards the reference temperature, covering a frequency range more significant than the limited range of the single sweep experiments, especially for higher angular frequencies. For a printing speed of 25 mm/s, the extrusion shear rate was 200 s^{-1}. The viscosity of Onyx at the printing temperature of 275 °C for this value of shear rate was 750 Pa×s, lower than that of acrylonitrile-styrene (ABS), equal to 1000 Pa×s, but higher than that of polylactic acid (PLA) equal to 200 Pa×s.

3.2 Dimensional analysis

To ensure dimensional stability, 40×4×15 mm^3 prismatic parts were realized in the same batch on the machine platform. After waiting eight hours to achieve the conditioned state, the samples were measured using a caliper to roughly match the dimensions. After verifying the absence of printing defects and an error of less than 2% on all main dimensions, a more precise measurement was done using a CMM. The total volume of a printed sample was calculated based on its actual geometry, using the average of five replicates. The errors made in the dimensions and geometry of these parts were usually systematic. The perimeters were filled continuously with specified layer thickness to realize the physical part. Since the whole object was fabricated layer-by-layer, the surface finish was poor because of the approximation of part surfaces into two-dimensional planer sections/layers. A volume deviation in MEX parts existed, known as volumetric error $V_\%$, computed as the difference between the volumes of deposited part V_p and the digital model V_d:
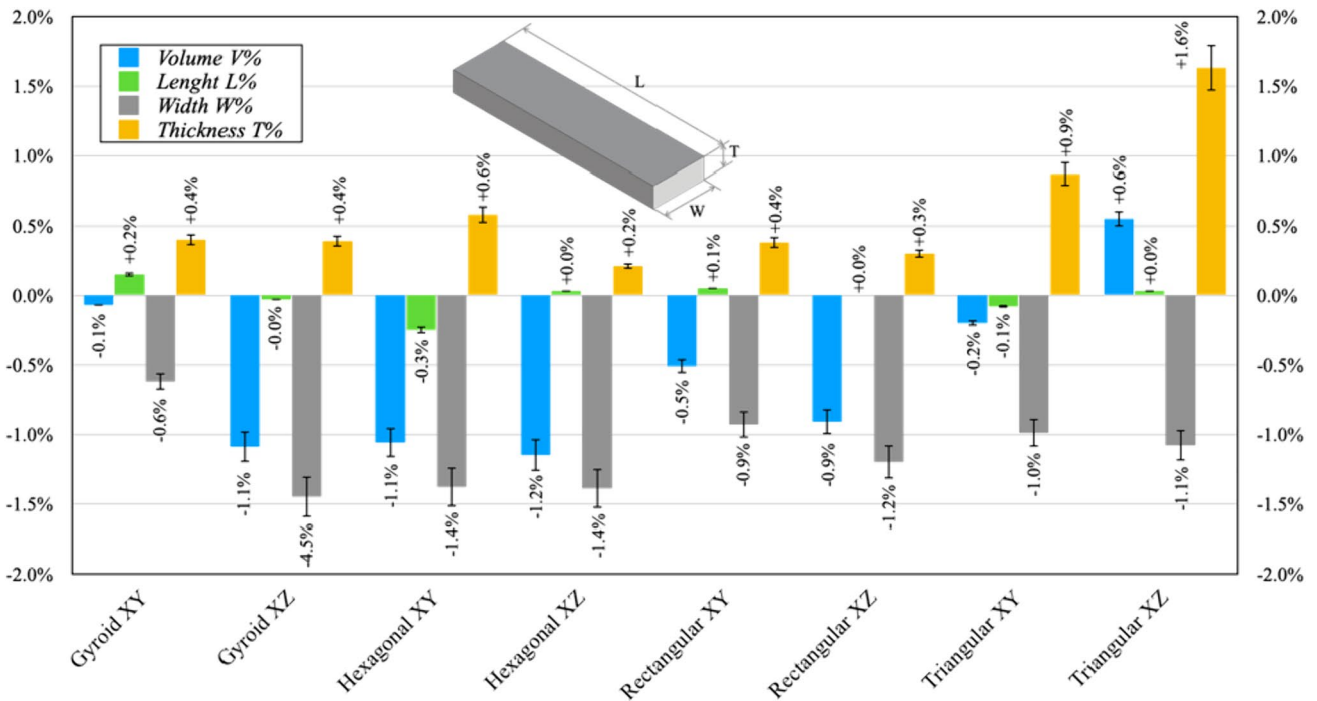
Fig. 6 Dimensional analysis

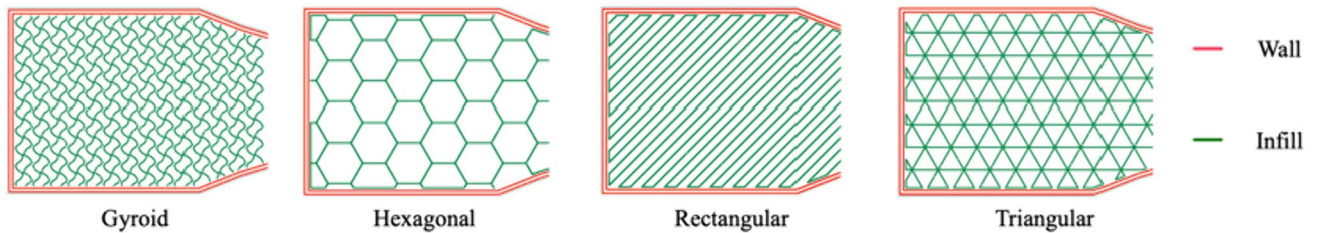**Fig. 7** Designation of the wall and infill lines for the various patterns

$$V_\% = \frac{V_p - V_d}{V_d}.$$ (2)

The results of the volumetric error $V_\%$ of the printed specimens are reported in Fig. 6. The other data in the same graph represent the deviation of length L, width W, and thickness T. The results showed that dimensional accuracy was high, below $\pm 2\%$ for each dimension and between $+0.5/-1.5\%$ for $V_\%$. The most accurate specimen was the flat gyroid infill, while the worst was the on-edge hexagonal infill. The significant error in the width dimension was independent of the build orientation.

Dimensional analyses were extended to the specimen patterns to appraise their accuracy. Figure 7 shows the 2D schemes for the different infill patterns, showing the type of lines estimated with the digital microscope. The deposited line, representing the line width, had a thickness of
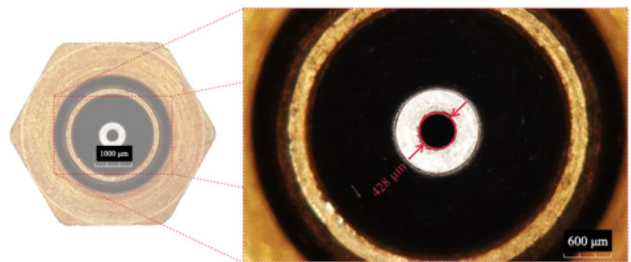

Fig. 8 Diameter of the FFF nozzle

80–120% of the nozzle diameter. The diameter of the FFF nozzle, shown in Fig. 8, was checked, obtaining a value of 430 ± 3.5 μm averaged on five measures. The infill was
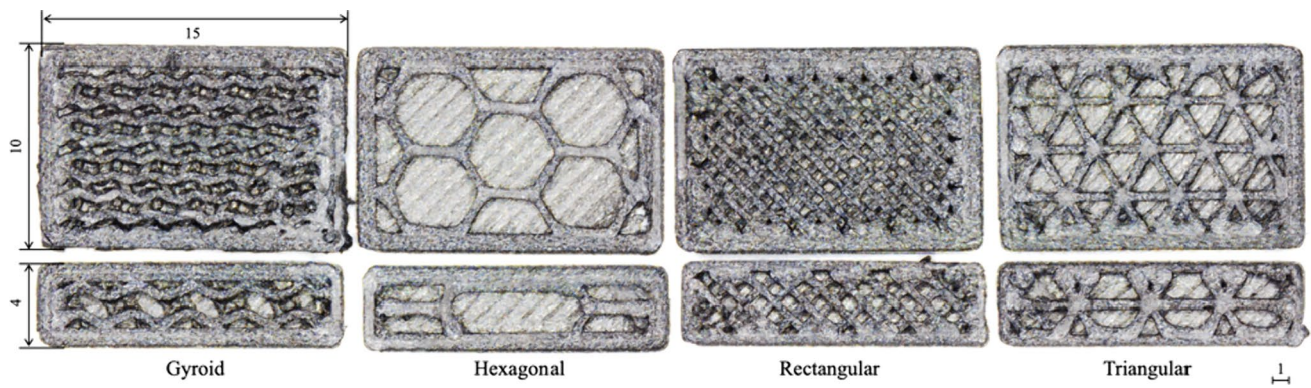
Fig. 9 Dimensional analysis of the infill patterns (all dimensions in mm)
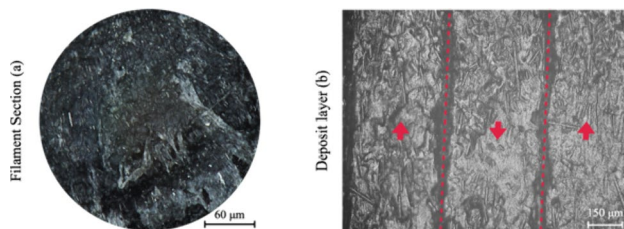

Fig. 10 Detail of the center section of the filament (**a**) and specimen section (**b**) observed with an optical microscope

created using individual lines (in green), while the perimeter walls (in red) comprised two adjacent deposited lines.

All infill patterns of the flat specimen were controlled, showing good dimensional accuracy in the perimeter and inner structure (Fig. 9). The variation in the deposition line width for each infill pattern was minimal, with a maximum value of less than 8%. The angle variation was very low, with a maximum value of 0.5%. The situation changed for the on-edge specimens due to the reduced section on the *XY* plane. All infills presented a flattened cell shape with a less thick perimeter, probably due to the slicer's internal adjustments on the flow rate. The gyroid pattern was the least influenced, while the most deformed was hexagonal.

The chopped carbon fiber in the material was also investigated. Figure 10a shows the arrangement of the chopped fiber in the filament before deposition. The fibers, with a diameter of 8.70 ± 0.13 μm and a length of 168 ± 37 μm, were oriented along the extrusion direction parallel to the filament axis, with a nonuniform distribution in the polymer phase. Some areas were fiber-rich, whereas others only presented the polymer matrix. This inhomogeneous distribution across the cross-section contributed to the local fiber volume fraction difference. Minor changes were detected after deposition, as shown in Fig. 10b. The black spaces represented the air gaps between deposition lines in a deposited layer. Most of the fibers were oriented along the moving direction

(red arrow). Identifying fiber orientation and volume fraction could be a key aspect in the performance analysis, because it greatly influenced the material properties, producing an increase in tensile strength more than twice and the elastic modulus seven times [27]. The deposition line presented a thickness of 0.408 mm and an uneven fiber distribution with polymer-rich areas alternated to high fiber-density regions.

3.3 Tensile tests

Tensile tests were carried out in two steps, according to the ISO 527:2019—plastics—determination of tensile properties. A first step was done with a strain gauge at a reduced speed (1 mm/min) to calculate Young's modulus and yield point, whereas a second phase was carried out at a higher speed (5 mm/min) to failure. Figure 11 shows the specimen and the extensometer mounting. Extensometers measured strain directly on the specimen, eliminating measurement influences from other testing components and increasing accuracy. This information was essential to compare the effect of the infill pattern.

The summary of tensile modulus E, yield strength σ_Y, and ultimate tensile strength UTS is reported in Table 3.

The curves of the tensile tests are reported in Fig. 12 of flat and on-edge specimens for a maximum strain equal to 20%. From a first analysis, the strength of the on-edge specimens was greater than that of flat specimens with the same infill patterns, confirming the outcomes of previous research [17, 18]. The strength performance, in terms of yield σ_Y and ultimate tensile strengths UTS, of tensile specimens with the gyroid infill was superior to other infill strategies for both orientations. This behavior could be due to the complex gyroid infill pattern and interlocking spiral shapes providing strength and support in all directions. The printed object was consequently less susceptible to warp, supporting higher stresses without rupture. On the contrary, the lowest performance characterized the hexagonal infill. The rectangular and the triangular infills
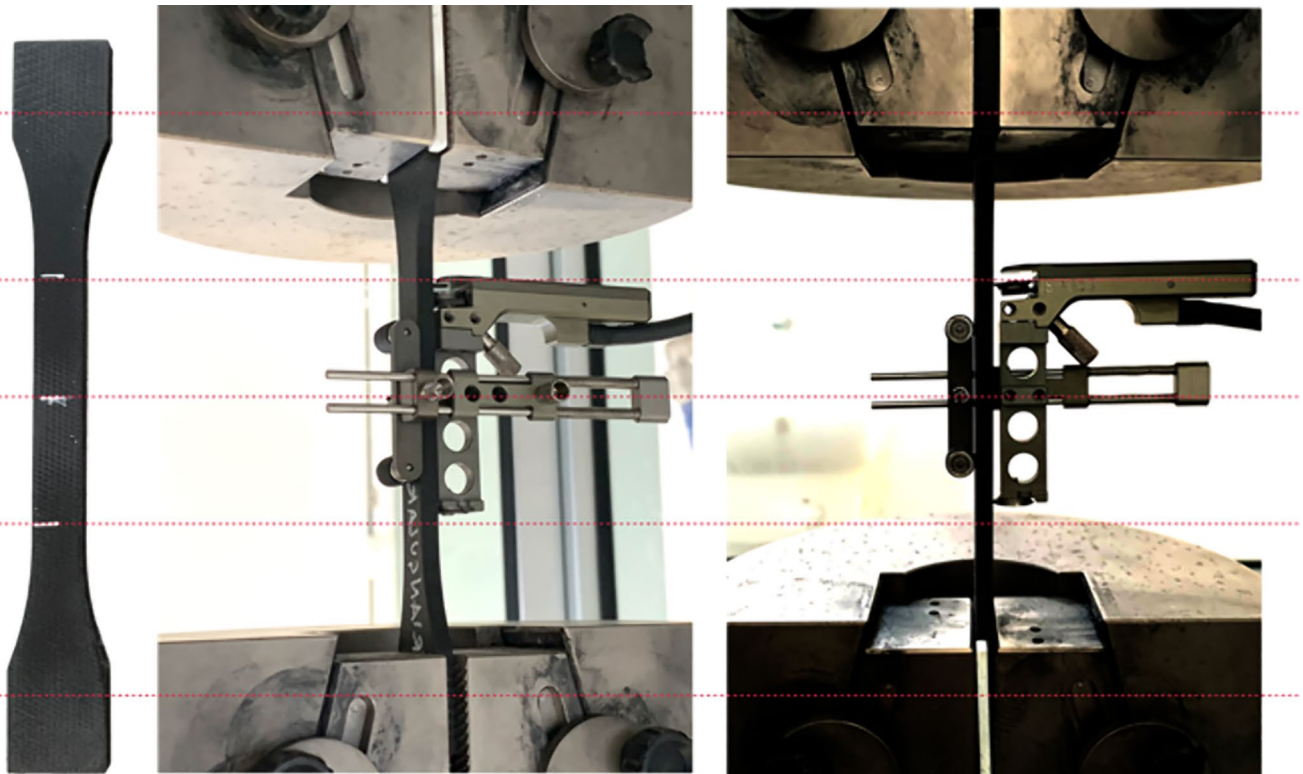
Fig. 11 Specimen mounted on the tensile test machine with the longitudinal extensometer

Table 3 Tensile specimens

Specimen ID	Build orientation	Tensile modulus E (MPa)	Yield strength σ_Y (MPa)	Ultimate tensile strength UTS (MPa)
Gyroid *XY*	Flat	871	18.29	51.30
Gyroid *XZ*	On-edge	1944	22.91	65.86
Hexagonal *XY*	Flat	1015	10.66	26.20
Hexagonal *XZ*	On-edge	2101	18.38	29.51
Rectangular *XY*	Flat	961	11.53	28.19
Rectangular *XZ*	On-edge	1835	21.58	47.87
Triangular *XY*	Flat	901	12.61	26.16
Triangular *XZ*	On-edge	1660	26.13	45.93

were almost equivalent, with intermediate results. Young modulus E showed a similar trend in the *XY* printing orientation, varying between 871 MPa (gyroid) and 1015 MPa (hexagonal). Young modulus values doubled in the *XZ* printing orientation, ranging between 1660 MPa (triangular) and 2100 MPa (hexagonal). The different printing orientations exhibited varying tensile properties due to two types of failures, one caused by layer separation and slippage and the other caused by single-layer breakage. The specimens printed along the *XY* and *XZ* directions exhibit a build direction parallel to the load during the test. All experimental strength and modulus values were 50% less

than samples with 100% infill. The analysis of variance (ANOVA) of the above data revealed that printing orientation and infill patterns were both influential, with a probability value (p value) less than 0.05. Figure 13 reports the plots of the main effects and interactions for the investigated response variables E, σ_Y, and UTS. A design point represented the measured value, whereas the ANOVA model computed the predicted point. The coefficient of determination R^2 of each response variable was higher than 98%, confirming an excellent agreement between measurements and predictions. Optimal results could be
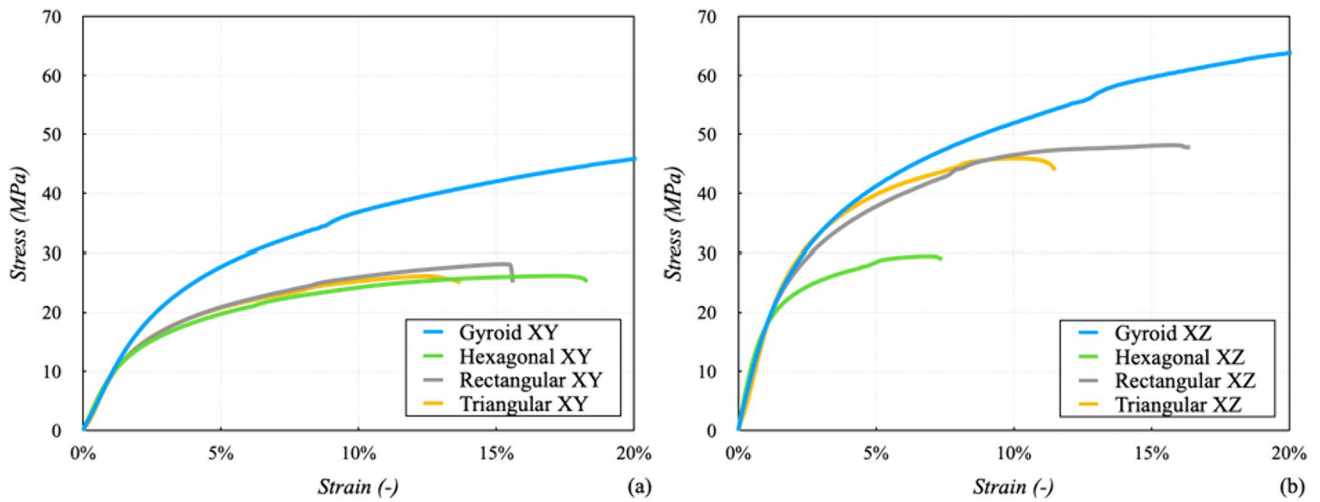
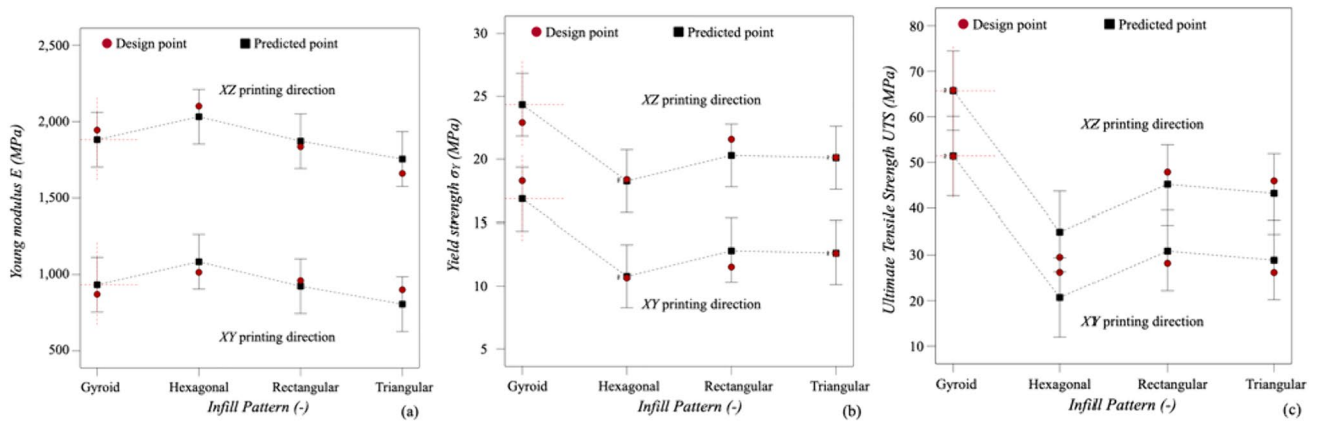**Fig. 12** Tensile test results for flat specimens (**a**) and on-edge specimens (**b**)

Fig. 13 Main effect and interaction plots of Young modulus (**a**), yield strength (**b**), and ultimate tensile strength (**c**)
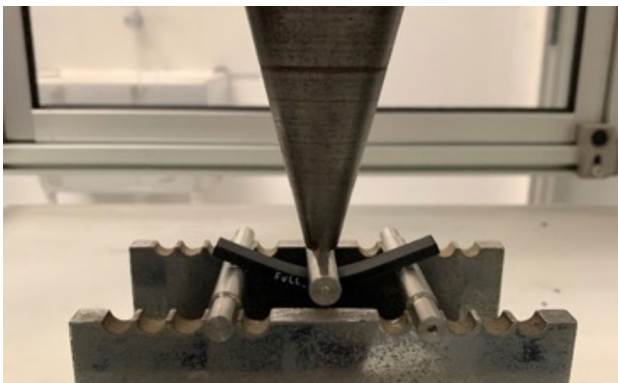

Fig. 14 Flexural test

achieved by printing the sample in the *XZ* direction using the gyroid infill pattern.

3.4 Flexural tests

The flexural tests were carried out following the ISO 178:2019—plastics—determination of flexural properties, Fig. 14. The specimen with dimensions $80 \times 10 \times 4$ mm³ was mounted with a span *L* between supports equal to 60 mm. The flexural strain and stress were

$$\varepsilon_f = \frac{6 \times s \times h}{L^2} \tag{3}$$

$$\sigma_f = \frac{3 \times F \times L}{2 \times b \times h^2}, \tag{4}$$

Table 4 Results of flexural tests

Specimen ID	Build orientation	Flexural modulus E_f (MPa)	Flexural stress σ_f (MPa)
Gyroid *XY*	Flat	1128	37.84
Gyroid *XZ*	On-edge	1774	47.23
Hexagonal *XY*	Flat	941	29.81
Hexagonal *XZ*	On-edge	1754	37.08
Rectangular *XY*	Flat	938	27.23
Rectangular *XZ*	On-edge	1367	34.66
Triangular *XY*	Flat	873	27.47
Triangular *XZ*	On-edge	1188	30.36

where s is deflection, h is thickness, and F is applied force. The flexural modulus E_f was computed using a linear regression applied to the stress–strain curve between the two flexural couples $(\varepsilon_{f1}, \sigma_{f1})$ and $(\varepsilon_{f2}, \sigma_{f2})$ with $\varepsilon_{f1} = 5 \times 10^{-3}$ and $\varepsilon_{f2} = 25 \times 10^{-3}$.

The summary of flexural modulus E_f and flexural strength σ_f is reported in Table 4. The curves of the flexural tests are reported in Fig. 15 of flat and on-edge specimens for a maximum strain equal to 12%.

From a first analysis, the strength of the on-edge specimens was greater than flat specimens with the same infill patterns, confirming the outcomes of tensile tests. The results were in agreement with those achieved in previous research [28]. The flexural strength σ_f of specimens with the gyroid infill was superior to other infill strategies for both orientations. This behavior demonstrated the efficiency of the complex gyroid infill pattern and interlocking spiral shapes, providing strength and support in all directions. On the contrary, the lowest performance characterized the triangular infill. The hexagonal and the rectangular infills were almost equivalent, with intermediate results. Flexural modulus E_f showed a similar trend in the *XY* printing orientation, varying between 873 MPa (triangular) and 1128 MPa (gyroid). Modulus values were 60% in the *XZ* printing orientation, ranging between 1118 MPa (triangular) and 1774 MPa (gyroid). All experimental strength and modulus values were 50% less than samples with 100% infill. The analysis of variance (ANOVA) of the above data revealed that printing orientation and infill patterns were both influential, with a probability value (p value) less than 0.05. Figure 16 reports the plots of the main effects and interactions for the investigated response variables E_f and σ_f. A design point represented the measured value, whereas the ANOVA model computed the predicted point. The coefficient of determination R^2 of each response variable was higher than 98%, confirming an excellent agreement between measurements and predictions. Optimal results could be achieved by printing the sample in the *XZ* direction using the gyroid infill pattern.

3.5 Time and cost analysis

A cost and production time analysis was carried out to analyze the trade-off with mechanical properties. A simple cost evaluation model was used to compute the final cost of the printed sample. The final cost was the sum of the material, labor, operation, and electricity costs. The material cost was defined as

$$\text{Material cost} = M \times p = \rho \times \pi \times (d/2)^2 \times L \times p, \quad (5)$$

where M was the part mass, p was the filament cost per kilogram, ρ the material density, and d and L were the filament diameter and deposited length. The labor cost was defined as
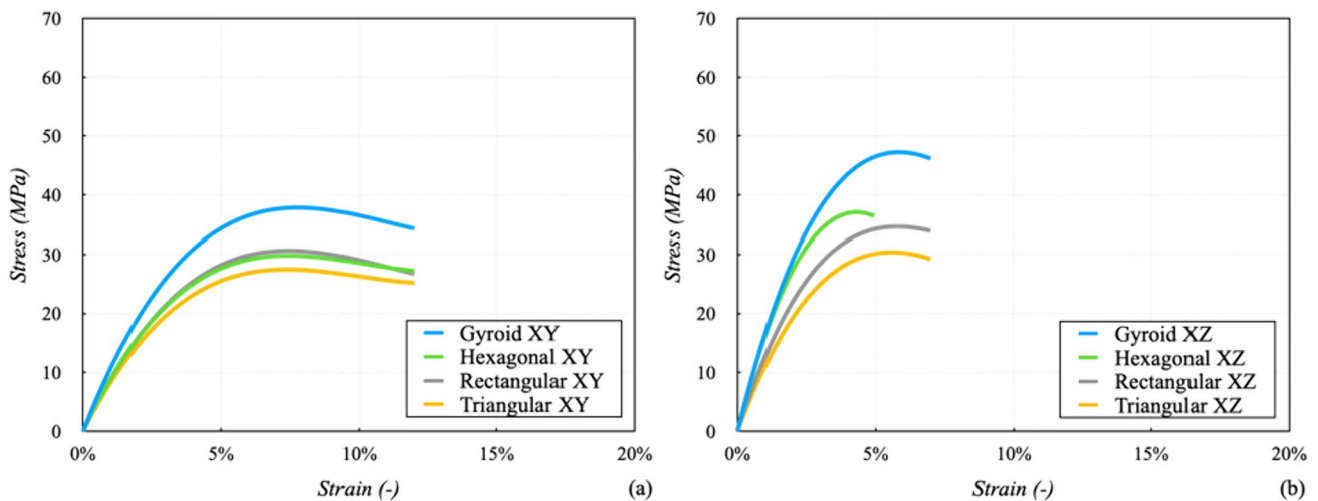

Fig. 15 Flexural test results for flat specimens (**a**) and on-edge specimens (**b**)
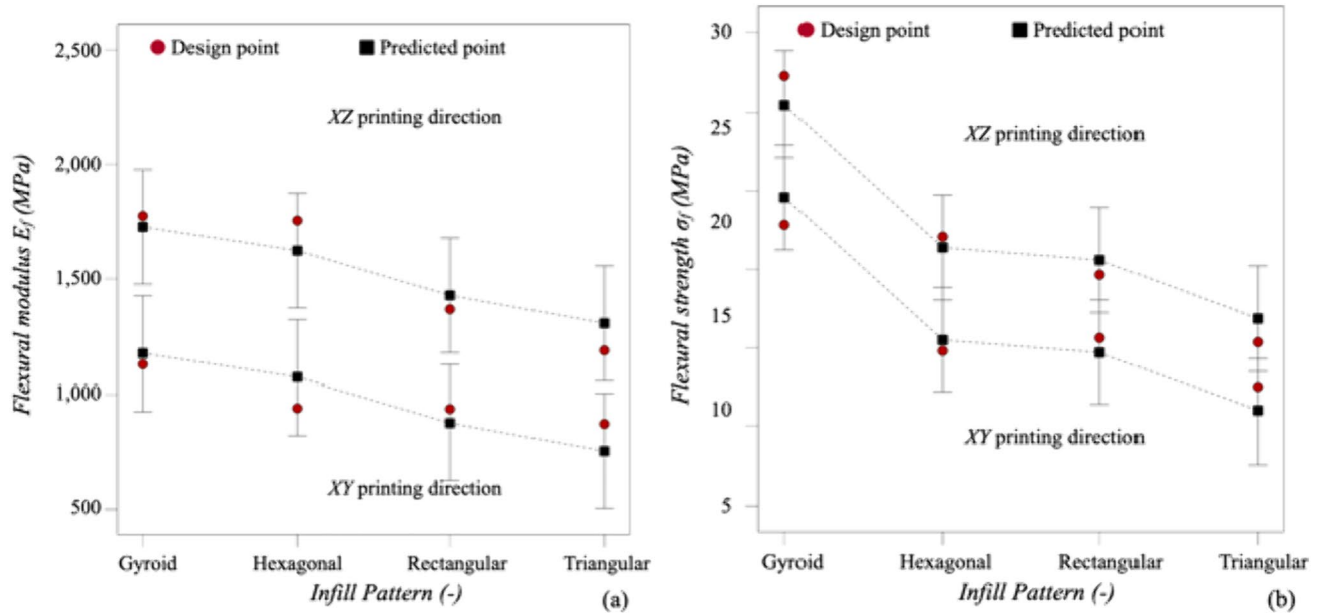
Fig. 16 Main effect and interaction plots of flexural modulus (**a**) and flexural strength (**b**)

Table 5 Cost specifications

Cost	Abbreviation	Value	Unit
Material price	p	287.5	USD/kg
Hourly labor rate	hlr	30	USD/h
Hourly operation charge	hoc	1	USD/h
Local electricity cost	lec	0.15	USD/kW

$$\text{Labor cost} = t_{\text{design}} \times \text{hlr}, \tag{6}$$

where t_{design} was the time to orient the part, set up printing parameters and slicing, and hlr was the hourly labor rate.

The operation cost was defined as

$$\text{Operation cost} = t_{\text{printing}} \times \text{hoc}, \tag{7}$$

where t_{printing} was the time needed to realize the part, and hoc was the hourly operation charge.

The electricity cost was

$$\text{Electricity cost} = t_{\text{printing}} \times \text{Pow} \times \text{lec}, \tag{8}$$

where Pow was the rated power of the MEX printer, and lec the local electricity cost. Table 5 reports the cost adopted.

For the tensile specimens printed along the *XY* plane, the minimum printing time was 52 min for the rectangular infill, and the maximum was 67 min for the gyroid infill. The cost variation was minimal, because the weight was very similar, varying between the minimum of the triangular specimen (7.7 USD) and the maximum of the gyroid (8.0 USD). For samples printed along the *XZ* plane,

neglecting time and cost for the supports, the minimum printing time was 75 min for the triangular, and the maximum was 92 min for the gyroid. Also, in this case, the cost variation was minimal, varying between the minimum of the rectangular (8.2 USD) and the maximum of the gyroid (8.5 USD). The difference in printing times was higher than the printing costs, independently of specimen printing orientation. The data of fully dense specimens were also reported in the graph, achieving 72 min and 9.1 USD for the flat specimen and 111 min and 9.9 USD for the on-edge sample. All data are shown in Fig. 17a. The trend of the flexural specimens was very similar to the tensile specimens, with an average cost savings of about 10% for almost all configurations to fully dense specimens. The average printing time of the flat specimen was 25 min, costing 6.13 USD, and 30 min and 6.26 USD for the on-edge specimen. All data are shown in Fig. 17b.

The analysis of variance (ANOVA) of the above data revealed that printing orientation and infill patterns were both influential, with a probability value (p value) less than 0.05. Figure 16 reports the plots of the main effects and interactions for the investigated response variables Final Cost %, as the ratio between the final cost of the specimen, tensile and flexural, with the selected infill compared to that with a full infill. A design point represented the measured value, whereas the ANOVA model computed the predicted point. The coefficient of determination R^2 of each response variable was higher than 97%, confirming an excellent agreement between measurements and predictions. The lowest cost could be achieved by printing the sample in the *XZ* direction using the triangular infill pattern. In contrast, the
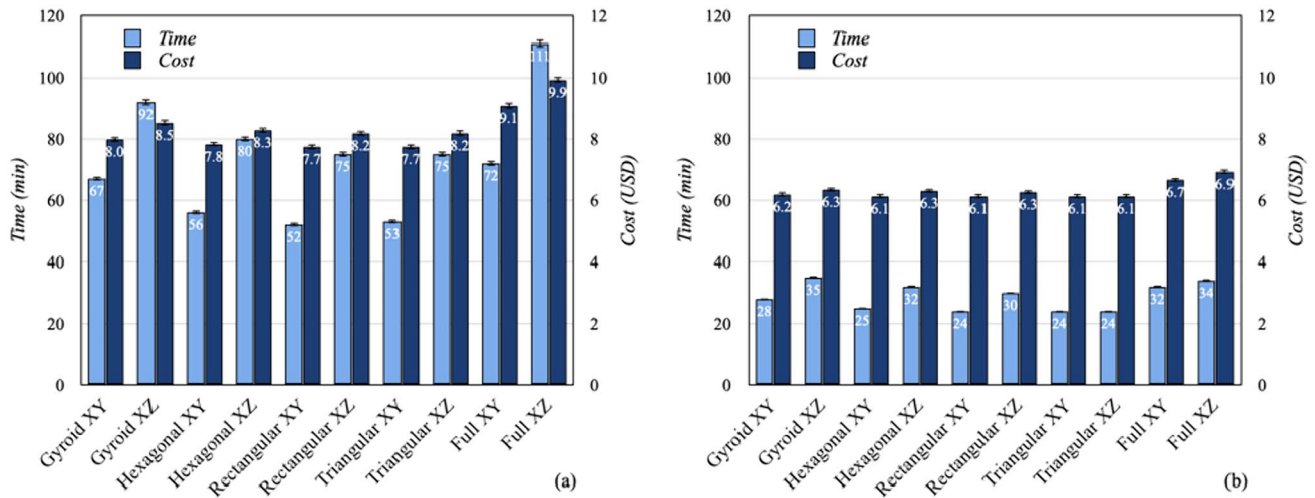
Fig. 17 Time and cost analysis graph of tensile (**a**) and flexural specimens (**b**)
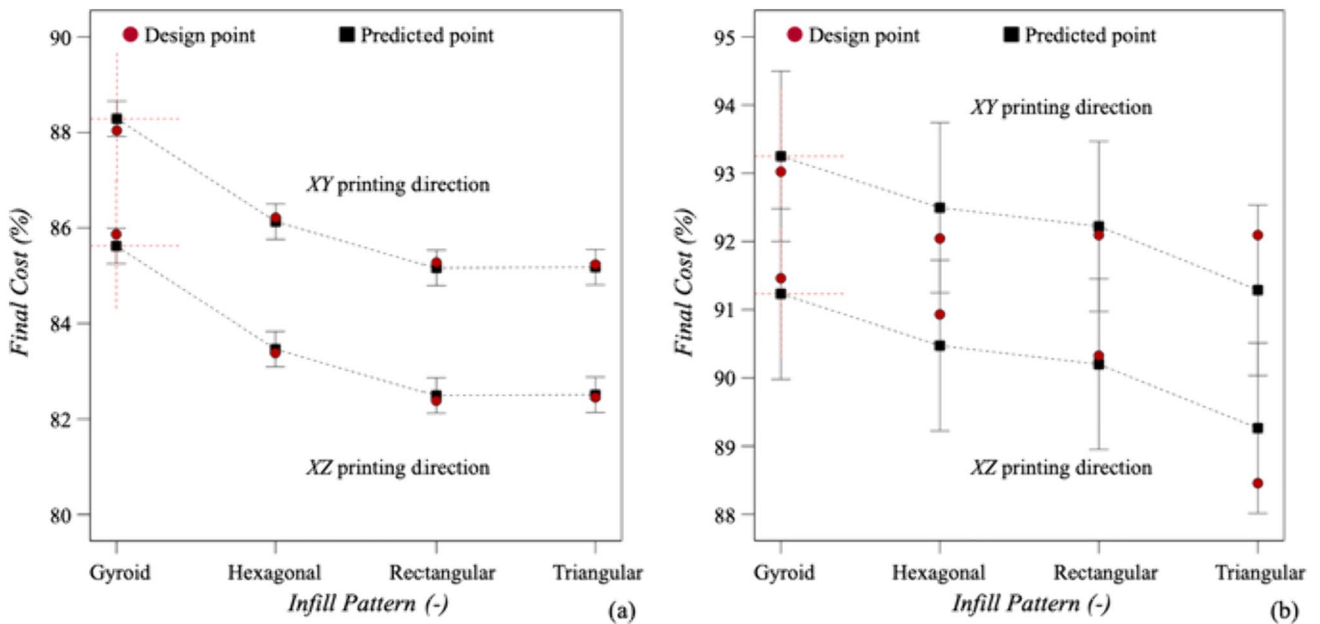

Fig. 18 Main effect and interaction plots of the final cost of tensile (**a**) and flexural specimens (**b**)

highest cost was associated with the specimen with gyroid infill printed in the *XY* direction. The comparison between cost and mechanical results indicated that higher strength and moduli values could be achieved with infill patterns requiring higher deposition time and, consequently, higher cost (Fig. 18).

4 Conclusions

This study aimed to analyze the tensile and flexural performance of Onyx specimens with different filling patterns and printing orientations and investigate the influence of these patterns on manufacturing time and cost. The results of the tensile tests showed that the gyroid-type infill was found to have the highest tensile strength, both in the case of print orientation along the *XY* and *XZ* planes. The second type of infill with higher tensile strength was the rectangular infill,

which was 1% lower in the printing orientation along *XY* and 11% lower in the printing orientation along *XZ* than the gyroid infill. The flexural tests revealed no significant difference in flexural strength, showing the specimen with gyroid infill as the best performer for both orientations. The specimens with triangular infill patterns provided the lowest performance. In addition, it was found that printing times and manufacturing costs varied depending on the infill pattern selected, with gyroid infill being an excellent alternative to rectangular infill due to its lower cost of printing, higher mechanical properties, and slightly longer printing times. The reason why the gyroid infill was better than the others could be found in its symmetrical nature on all three axes, which resulted in specimens that were 3% lighter than rectangular specimens on the *XY* plane and 14% lighter on the *XZ* plane. Overall, this study has contributed to a better understanding of the performance of different filling patterns and printing orientations in Onyx printing and has provided valuable insights into the trade-offs between mechanical properties, cost, and time. The findings can guide the selection of infill patterns and printing orientations for different applications and optimize the manufacturing process of Onyx printing.

Availability of data and materials The raw data are available upon reasonable request from the corresponding author.

Declarations

Conflict of interest The authors declare no competing interests.

Award numbers Law number 232/2016 (Grant No. CUP—D93C23000100001) and PE00000004, Concession Decree No. 1551 of 11/10/2022 of the Italian Ministry of University and Research, CUP D93C22000920001, MICS (Made in Italy—Circular and Sustainable).

References

1. Ferreira M, Machado F, Alves ATM (2019) A review on fibre reinforced composite printing via FFF. Rapid Prototyp J 25:972–988. https://doi.org/10.1108/RPJ-01-2019-0004

2. Kabir SMF, Mathur K, Seyam AFM (2020) A critical review on 3D printed continuous fiber-reinforced composites: history, mechanism, materials, and properties. Compos Struct 232:111476. https://doi.org/10.1016/j.compstruct.2019.111476

3. Frketic J, Dickens T, Ramakrishnan S (2017) Automated manufacturing and processing of fiber-reinforced polymer (FRP) composites: an additive review of contemporary and modern techniques for advanced materials manufacturing. Addit Manuf 14:69–86. https://doi.org/10.1016/j.addma.2017.01.003

4. Wong J, Altassan A, Rosen DW (2023) Additive manufacturing of fiber-reinforced polymer composites: a technical review and status of design methodologies. Compos B Eng 255:110603. https://doi.org/10.1016/j.compositesb.2023.110603

5. Blok LG, Longana ML, Yu H, Woods BKS (2018) An investigation into 3D printing of fibre reinforced thermoplastic composites. Addit Manuf 22:176–186. https://doi.org/10.1016/j.addma.2018.04.039

6. Fernandes RR, Tamijani AY, Al-Haik M (2021) Mechanical characterization of additively manufactured fiber-reinforced composites. Aerosp Sci Technol 113:106653. https://doi.org/10.1016/j.ast.2021.106653

7. Wang X, Jiang M, Zhou Z, Gou J, Hui D (2017) 3D printing of polymer matrix composites: a review and prospective. Compos B Eng 110:442–458. https://doi.org/10.1016/j.compositesb.2016.11.034

8. Hofstätter T, Pedersen DB, Tosello G, Hansen HN (2017) State-of-the-art of fiber-reinforced polymers in additive manufacturing technologies. J Reinf Plast Compos 36:1061–1073. https://doi.org/10.1177/0731684417695648

9. Prajapati AR, Dave HK, Raval HK (2021) Effect of fiber volume fraction on the impact strength of fiber reinforced polymer composites made by FDM process. Mater Today Proc 44:2102–2106. https://doi.org/10.1016/j.matpr.2020.12.262

10. Krzikalla D et al (2022) On flexural properties of additive manufactured composites: experimental, and numerical study. Compos Sci Technol. https://doi.org/10.1016/j.compscitech.2021.109182

11. Pratama J et al (2021) A review on reinforcement methods for polymeric materials processed using fused filament fabrication (FFF). Polymers 13:4022. https://doi.org/10.3390/polym13224022

12. Lubombo C, Huneault MA (2018) Effect of infill patterns on the mechanical performance of lightweight 3D-printed cellular PLA parts. Mater Today Commun 17:214–228. https://doi.org/10.1016/j.mtcomm.2018.09.017

13. Dorčiak F et al (2019) Tensile test for specimen with different size and shape of inner structures created by 3D printing. Transp Res Procedia 40:671–677. https://doi.org/10.1016/j.trpro.2019.07.095

14. Bárnik F et al (2019) Comparing mechanical properties of composites structures on Onyx base with different density and shape of fill. Transp Res Procedia 40:616–622. https://doi.org/10.1016/j.trpro.2019.07.088

15. Ahmadifar M et al (2022) Mechanical behavior of polymer-based composites using fused filament fabrication under monotonic and fatigue loadings. Polym Polym Compos 30:096739112210824. https://doi.org/10.1177/09673911221082480

16. Akhil VM et al (2022) Experimental investigations on the effect of infill patterns on PLA for structural applications. Mater Today Proc. https://doi.org/10.1016/j.matpr.2022.10.292

17. Zhou J et al (2023) Comparison of different quasi-static loading conditions of additively manufactured composite hexagonal and auxetic cellular structures. Int J Mech Sci. https://doi.org/10.1016/j.ijmecsci.2022.108054

18. Pipalla R, Schuster J, Shaik YP (2021) Experimental analysis on 3D printed onyx specimens with honeycomb infill structure. J Adv Mat Sci Eng. https://doi.org/10.33425/2771-666x.1003

19. Wang K et al (2020) Effects of infill characteristics and strain rate on the deformation and failure properties of additively manufactured polyamide-based composite structures. Results Phys. https://doi.org/10.1016/j.rinp.2020.103346

20. Ali Z et al (2023) Effect of infill density, build direction and heat treatment on the tensile mechanical properties of 3D-printed carbon-fiber nylon composites. Compos Struct. https://doi.org/10.1016/j.compstruct.2022.116370

21. Spina R, Cavalcante B (2020) Evaluation of grinding of unfilled and glass fiber reinforced polyamide 6,6. Polymers. https://doi.org/10.3390/polym12102288

22. Material Datasheet Composites. https://markforged.com/it/materials/plastics/onyx. Accessed 01 2024

23. Whang C et al (2024) Mechanical and tribological properties of FDM-printed polyamide. Tribol Int. https://doi.org/10.1016/j.triboint.2023.109198

24. Spina R, Cavalcante B (2021) Hygromechanical performance of polyamide specimens made with fused filament fabrication. Polymers. https://doi.org/10.3390/polym13152401

25. Spina R (2019) Performance analysis of colored PLA products with a fused filament fabrication process. Polymers. https://doi.org/10.3390/polym11121984

26. (2012) PA-6 polyamide-6. Handbook of Polymers. https://doi.org/10.1016/B978-1-895198-47-8.50069-2

27. Seta B et al (2023) Modeling fiber orientation and strand shape morphology in three-dimensional material extrusion additive manufacturing. Compos Part B. https://doi.org/10.1016/j.compositesb.2023.110957

28. Barnik V et al (2019) Comparing mechanical properties of composites structures on Onyx base with different density and shape of fill. Transp Res Procedia 40(616):622. https://doi.org/10.1016/j.trpro.2019.07.088